RESEARCH ARTICLE

Magnetic Resonance in Medicine

Highly accelerated EPI with wave encoding and multi-shot simultaneous multislice imaging

Jaejin Cho[1,2] | Congyu Liao[3,4] | Qiyuan Tian[1,2] | Zijing Zhang[5] | Jinmin Xu[5] | Wei-Ching Lo[6] | Benedikt A. Poser[7] | V. Andrew Stenger[8] | Jason Stockmann[1,2,9] | Kawin Setsompop[3,4] | Berkin Bilgic[1,2,9]

[1]Athinoula A. Martinos Center for Biomedical Imaging, Massachusetts General Hospital, Boston, Massachusetts, USA

[2]Harvard Medical School, Boston, Massachusetts, USA

[3]Radiological Sciences Laboratory, Department of Radiology, Stanford University, Stanford, California, USA

[4]Department of Electrical Engineering, Stanford University, Stanford, California, USA

[5]State Key Laboratory of Modern Optical Instrumentation, College of Optical Science and Engineering, Zhejiang University, Hangzhou, China

[6]Siemens Medical Solutions, Boston, Massachusetts, USA

[7]Maastricht Brain Imaging Center, Faculty of Psychology and Neuroscience, Maastricht University, Maastricht, The Netherlands

[8]MR Research Program, Department of Medicine, John A. Burns School of Medicine, University of Hawai'i, Honolulu, Hawaii, USA

[9]Harvard-MIT Health Sciences and Technology, Massachusetts Institute of Technology, Cambridge, Massachusetts, USA

Correspondence
Qiyuan Tian, Athinoula A. Martinos Center for Biomedical Imaging, Massachusetts General Hospital, Building 149, Room 2301, 13th Street, Charlestown, MA, 02129, USA.
Email: qtian@mgh.harvard.edu

Purpose: To introduce wave-encoded acquisition and reconstruction techniques for highly accelerated EPI with reduced g-factor penalty and image artifacts.

Theory and Methods: Wave-EPI involves application of sinusoidal gradients during the EPI readout, which spreads the aliasing in all spatial directions, thereby taking better advantage of 3D coil sensitivity profiles. The amount of voxel spreading that can be achieved by the wave gradients during the short EPI readout period is constrained by the slew rate of the gradient coils and peripheral nerve stimulation monitor. We propose to use a "half-cycle" sinusoidal gradient to increase the amount of voxel spreading that can be achieved while respecting the slew and stimulation constraints. Extending wave-EPI to multi-shot acquisition minimizes geometric distortion and voxel blurring at high in-plane resolutions, while structured low-rank regularization mitigates shot-to-shot phase variations. To address gradient imperfections, we propose to use different point spread functions for the k-space lines with positive and negative polarities, which are calibrated with a FLEET-based reference scan.

Results: Wave-EPI enabled whole-brain single-shot gradient-echo (GE) and multi-shot spin-echo (SE) EPI acquisitions at high acceleration factors at 3T and was combined with g-Slider encoding to boost the SNR level in 1 mm isotropic diffusion imaging. Relative to blipped-CAIPI, wave-EPI reduced average and maximum g-factors by up to 1.21- and 1.37-fold at $R_{in} \times R_{sms} = 3 \times 3$, respectively.

Conclusion: Wave-EPI allows highly accelerated single- and multi-shot EPI with reduced g-factor and artifacts and may facilitate clinical and neuroscientific applications of EPI by improving the spatial and temporal resolution in functional and diffusion imaging.

KEYWORDS

diffusion imaging, functional imaging, g-Slider, low-rank reconstruction, multi-shot EPI, parallel imaging, SMS imaging, wave-CAIPI, wave-EPI

1 | INTRODUCTION

EPI provides fast encoding per imaging slice and has found wide application in clinical and neuroscientific acquisitions,[1–3] especially in functional (fMRI) and diffusion (dMRI) imaging.[4,5] However, single-shot EPI suffers from severe susceptibility-induced geometric distortion and T_2- and T_2*-induced voxel blurring due to low bandwidth along the phase-encoding direction.[6,7] These artifacts only get worse at higher in-plane resolution as the time it takes to acquire each line of k-space increases approximately linearly.

In-plane parallel imaging (PI) acceleration is an effective approach to mitigating EPI-related artifacts by reducing the effective echo spacing.[8–10] Existing PI approaches aim to achieve high accelerations by exploiting linear dependencies across the multi-coil data, either through interpolation across k-space (e.g., GRAPPA[11]), or image-space reconstruction using a pre-calculated coil sensitivity map (e.g., SENSE[12]). More recent work, ESPIRiT, has helped bridge the gap between GRAPPA and SENSE.[13]

Another approach to mitigate EPI-related artifacts is multi-shot (MS-) acquisition. This also provides a reduction in effective echo spacing by segmenting the k-space into multiple portions which are covered across multiple TRs. However, potential shot-to-shot phase variations across multiple EPI shots may lead to additional artifacts.[14–16] Recent algorithms including multiplexed sensitivity encoding (MUSE[17]) and multi-shot sensitivity encoded diffusion data recovery using structured low-rank matrix completion (MUSSELS[18]) allow for successful and navigator-free combination of these shots. MUSE achieves this by estimating phase variations from interim shot images and incorporating these into a final joint SENSE reconstruction where all the shot data are combined. MUSSELS jointly reconstructs MS-EPI images using Hankel structured low-rank constraint across the EPI shots. Similar structured low-rank priors have also been previously explored in LORAKS,[19,20] SAKE,[21] and ALOHA[22] for image reconstruction in spin-warp

acquisitions as well as Nyquist ghost correction[23,24] in EPI.

Simultaneous multislice (SMS) acquisition excites and encodes multiple imaging slices simultaneously to offer a significant reduction in TR.[25–28] Controlled aliasing in parallel imaging (CAIPI) modulates the phase of excited slices in k-space to improve the PI conditioning for resolving collapsed slice data.[29] This phase modulation induces inter-slice shifts in the phase encoding (PE) direction so that image aliasing is distributed in both PE and slice dimensions. Blipped-CAIPI extends the CAIPI strategy to echo-planar trajectories.[30] This modulates the phase of the excited slices by using small gradient-blips in the slice-selection direction during ramp-time between the adjacent readouts to create inter-slice shifts in the PE direction.

Wave-CAIPI is a more recent controlled aliasing method that can further reduce noise amplification and aliasing artifacts.[31,32] It uses extra sinusoidal gradient modulations in the phase- and the partition-encoding directions during the readout to better harness coil sensitivity variations in all three dimensions. Wave encoding also incorporates 2D-CAIPI inter-slice shifts to improve the PI conditioning[33] and has found applications in highly accelerated gradient echo (GE), MPRAGE, and fast spin echo acquisitions.[32,34–37]

We had previously combined wave encoding with EPI readout for GE contrast and demonstrated high in-plane acceleration to reduce geometric distortion and T_2* blurring in earlier ISMRM proceedings.[38–41] In this work, we report improvements in calibration, acquisition, and reconstruction strategies for wave-EPI. Specifically,

1. We use different point spread functions (PSFs) to represent the voxel spreading effect of sinusoidal gradients for the k-space lines with positive and negative polarities. This "dual PSF" approach allows us to address potential imperfections in all three gradient axes. We estimate these PSFs from rapid calibration scans with FLEET acquisition ordering.[42]

2. The amount of voxel spreading that can be achieved by the wave gradients during the short EPI readout is constrained by the slew rate and the peripheral nerve stimulation (PNS) limit. We propose to increase the amount of voxel spreading using a "half-cycle" sinusoidal.

3. We incorporate SMS encoding to improve efficiency, and MS capability to further reduce distortion and T_2/T_2^*-induced voxel blurring. We extend these capabilities to spin echo (SE) and diffusion contrasts. Incorporating structured low-rank regularization allows for leveraging the similarities across the shots for improved reconstruction and accounts for potential shot-to-shot phase differences.

4. We take advantage of the SNR benefit provided by the volumetric noise averaging in the RF-encoded g-Slider approach,[43] and push the spatial resolution in wave-EPI acquisition. We propose a joint image reconstruction method that incorporates g-Slider slab encoding operator into the wave-EPI forward model to minimize potential resolution loss due to an intravoxel blurring effect from wave gradients.

These improvements allowed us to demonstrate up to 1.21- and 1.37-fold gain in average and maximum g-factor noise amplification over blipped-CAIPI for single-shot GE-EPI using a 32-channel head coil at $R_{in} \times R_{sms} = 3 \times 3$. Wave-EPI provided marked improvement in image quality at the high acceleration rate of $R_{in} \times R_{sms} = 5 \times 2$-fold *per shot* in diffusion acquisition using two shots of EPI. Further, we demonstrate high resolution diffusion data at 1 mm isotropic voxel size by combining g-Slider with wave-EPI at $R_{in} \times R_{sms} = 6 \times 2$-fold acceleration using two EPI shots with high SNR and geometric fidelity and improved g-factor mitigation.

2 | THEORY

2.1 | Voxel spreading by wave-encoding

Wave-encoding uses additional sinusoidal gradients during the readout to take better advantage of 3D coil sensitivity profiles.[31] Wave-encoding modulates the phase during the readout and incurs a corkscrew trajectory in k-space. The wave-encoded signal, s, can be explained using the following equation.

$$s(t) = \int_{x,y,z} m(x,y,z) e^{-i2\pi\left(k_x(t)x + k_y y + k_z z\right)} e^{-i\gamma \int_0^t \left(g_y(\tau)y + g_z(\tau)z\right)d\tau} dxdydz \quad (1)$$

where m is the magnetization, γ is the gyromagnetic ratio, and g is the time-varying sinusoidal wave gradient. The

voxel signal displacement can be defined by the phase modulation of wave-encoding over k_x as follows.

$$s(t) = \int_{x,y,z} m(x,y,z) e^{-i2\pi\left(k_x(t)(x+d(t,y,z)) + k_y y + k_z z\right)} dxdydz \quad (2)$$

$$\text{where } d(t,y,z) = \frac{\gamma \int_0^t \left(g_y(\tau)y + g_z(\tau)z\right) d\tau}{2\pi k_x(t)}. \quad (3)$$

Voxel spreading by wave-encoding, $d(t,y,z)$, is a function of readout time and the position in the y- and z-dimensions, which distributes aliasing in three dimensions in accelerated acquisitions.

2.2 | Limited voxel spreading in EPI acquisition

In EPI acquisition, the maximum amount of signal displacement is limited by the short readout window. To explain the relation between signal displacement and the readout duration, we first describe the signal displacement by cosine wave-encoding in the y direction as follows.

$$
\begin{aligned}
d(t,y) &= y \cdot \frac{\gamma \int_0^t g_y(\tau)d\tau}{2\pi k_x(t)} \\
&= y \cdot \frac{1}{2\pi} \cdot \frac{\int_0^t G_w \cos\left(2\pi \frac{n_c}{T_r}\tau\right) d\tau}{G_x t} \\
&= y \cdot \frac{1}{2\pi} \cdot \frac{G_w}{G_x} \cdot \frac{\sin\left(2\pi \frac{n_c}{T_r} t\right)}{2\pi \frac{n_c}{T_r} t} \\
&= y \cdot \frac{1}{2\pi} \cdot \frac{G_w}{G_x} \cdot sinc\left(2\pi \frac{n_c}{T_r} t\right) \quad (4)
\end{aligned}
$$

where T_r is the duration of the readout window, n_c is the number of wave cycles, G_w is the amplitude of the cosine wave-encoding gradient, and G_x is the amplitude of the readout gradient. The maximum of G_w is constrained by the slew rate of the gradient coil, R_{max}, due to:

$$G_w \leq \frac{R_{max} T_r}{2\pi n_c}. \quad (5)$$

The voxel spreading can be described using R_{max}, T_r, and n_c as follows.

$$d(t,y) \leq y \cdot \frac{1}{2\pi} \cdot \frac{1}{G_x} \cdot \frac{R_{max} T_r}{2\pi n_c} \cdot sinc\left(2\pi \frac{n_c}{T_r} t\right). \quad (6)$$

Increasing T_r can maximize voxel spreading and improve conditioning of parallel imaging reconstruction. However, in EPI acquisition, high receiver bandwidth is required to mitigate EPI-related artifacts by reducing echo spacing time, which limits the achievable voxel spreading. The

spreading incurred by the sine wave-encoding in the z direction is similarly limited. In Equation (6), most of the variables are constrained by FOV, hardware specifications and receiver bandwidth; only n_c can be adjusted. In this paper, we increase the maximum voxel spreading by minimizing n_c while maintaining a high receiver bandwidth in EPI acquisition. We chose a "half-cycle" cosine and one cycle sine wave-encoding in the y and z directions, respectively.

3 | METHODS

3.1 | Wave-EPI

Wave-CAIPI strategy was applied to EPI readout to mitigate geometric distortion and T_2 and/or T_2^* blurring by minimizing the effective echo spacing with high in-plane undersampling and reduce the TR using multiband acceleration. Figure 1A shows the proposed wave-SE-EPI sequence diagram, where "half-cycle" of cosine wave gradients and one-cycle of sine wave gradients were applied in the phase encoding and the slice-selection directions, respectively. This creates the usual corkscrew wave trajectory as shown in Figure 1B, but doubles the amplitude in the phase-encoding sinusoidal in the presence of stringent slew rate limitations, provided that the PNS limit is not exceeded. Because the polarity of the readout gradient is alternating between even and odd EPI readouts, the polarity of the cosine wave-gradients is also flipped to

maintain the consistency of the k-space trajectory of the wave-EPI sequence.

3.2 | Dual PSF and calibration scan

Wave-PSFs are expected to be applied in the x direction via convolution operator, but we multiply the Fourier transform of wave-PSFs in the k_x domain for convenience. Because eddy currents and system imperfections can create differences between the actual and theoretical wave-PSFs, accurate characterization of the actual k-space trajectory is needed. In addition, wave-encoding gradients are continuously flipping their polarity to maintain the trajectory consistency in k-space, as a result, the positive and negative readouts may have different PSFs due to such imperfections. We propose to calibrate and use the Fourier transform of "dual" wave-PSFs to de-convolve the positive and negative readouts as shown in Figure 2A.

To estimate the experimental PSF, we developed a reference scan based on the fast low-angle excitation echo-planar technique (FLEET) with and without wave-encoding.[42] Reference scans were acquired twice with opposite readout gradient-polarities[44] to estimate PSFs in both positive and negative polarities. The Fourier transform of wave-PSFs can be directly calculated from the phase difference between calibration data with and without wave-encoding in the k_x-y or k_x-z hybrid domain. However, due to low-flip angle excitation, this direct approach may suffer from low SNR, especially in
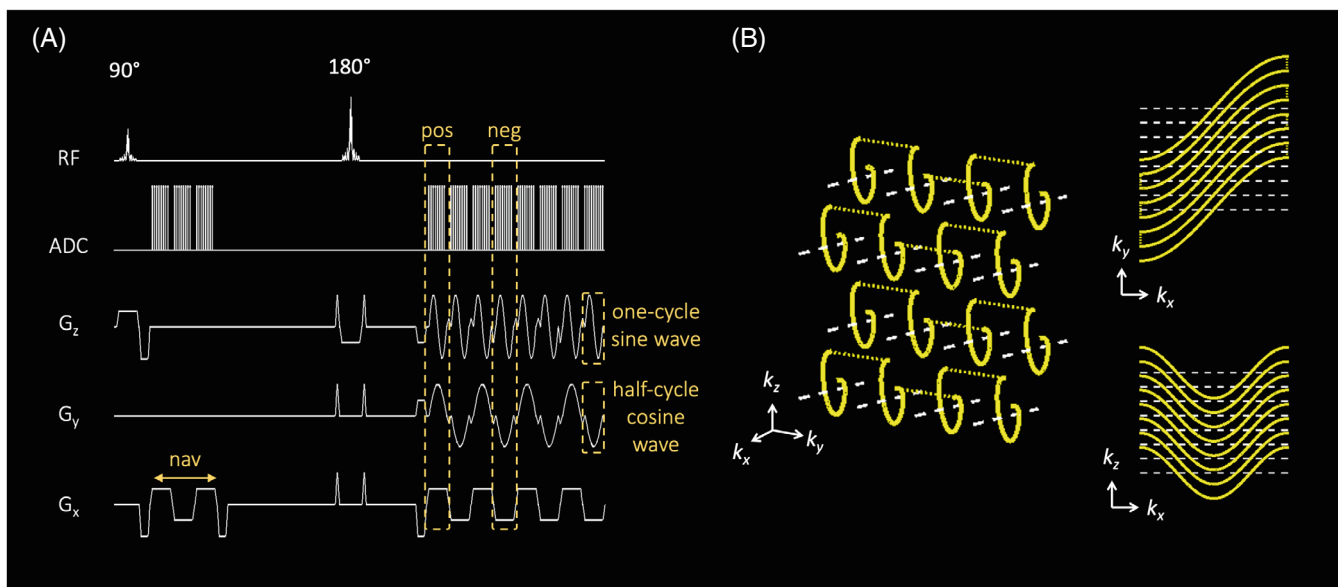
FIGURE 1 A, The proposed wave-EPI based on SE-EPI. Half-cycle of cosine wave-encoding and one-cycle of sine wave-encoding were applied in the phase-encoding and the slice-selection directions, respectively. B, Wave-EPI trajectory in k-space
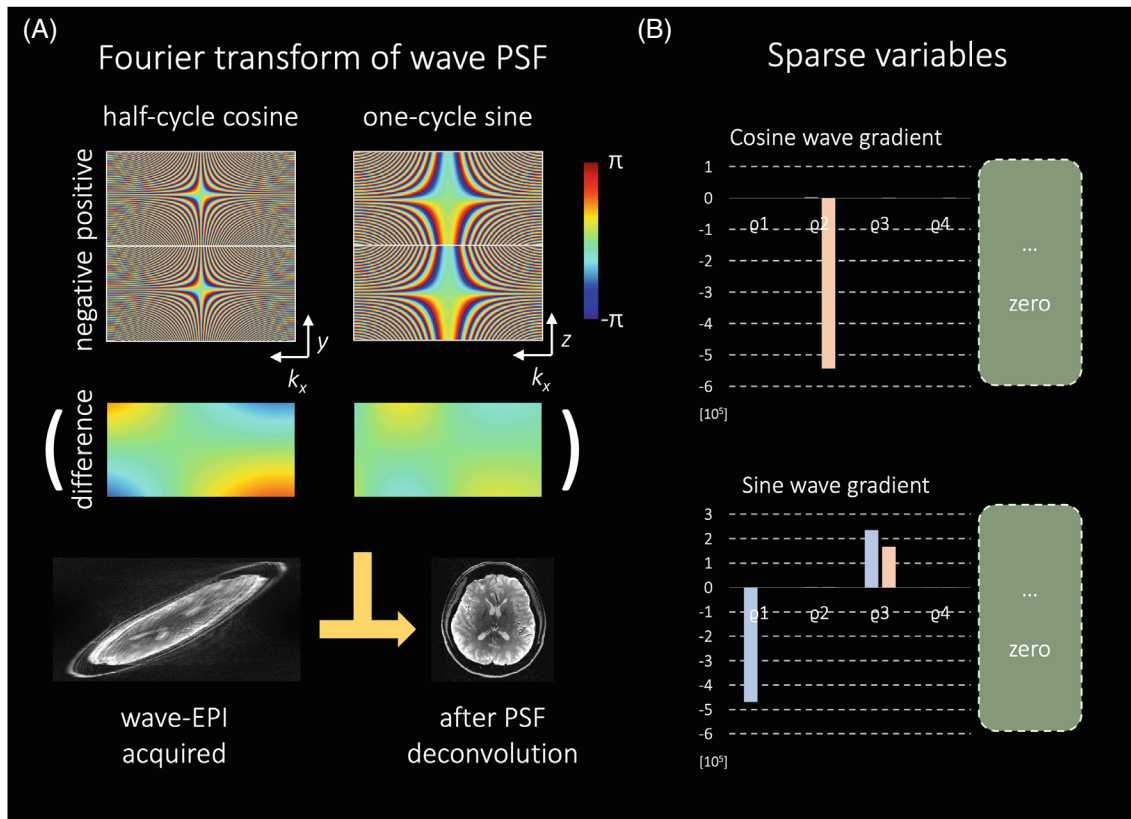
FIGURE 2 A. The concept of the wave-encoding deconvolution using Fourier transform of the dual wave-PSFs. B. The sparse variables indicating Fourier transform coefficients of the spatial frequency by wave encoding. (blue) real values (orange) imaginary values.

high-frequency regions. Therefore, we use a sparse frequency approach called "auto-PSF" to estimate PSFs in the high k_x regions.[45] The auto-PSF technique assumes that the wave-encoding gradient has sparse frequency content in the Fourier-transformed domain due to its sinusoidal shape, therefore, only a small number of frequency variables is needed to represent wave-encoding. Figure 2B shows the sparse variables indicating the Fourier transform coefficients of the spatial frequency by wave-encoding gradients. Instead of fitting the entire wave-encoding trajectory, we looked for the sparse frequency variables to estimate the wave-PSF as follows.

$$\varrho = \underset{\varrho}{\mathrm{argmin}} \left(\left\| \mathcal{F}_y P(\varrho) \mathcal{F}_y^{-1} S_r - S_w \right\|_2^2 \right) \quad (7)$$

where ϱ are the sparse frequency variables representing wave-encoding in its Fourier-transformed domain, P is the wave-PSF generator using the sparse frequency variables, S_r is the k-space reference signal without wave-encoding, and S_w is the k-space reference signal with wave-encoding, respectively. In this paper, ϱ only has the four complex numbers to present the wave-encoding. We separately estimated ϱ for each positive and negative EPI readout as well as each gradient in the y and z direction. As a result, the

Fourier transforms of four different PSFs are calibrated as shown in Figure 2A. Supporting Information Figure S1, which is available online, shows the auto-PSF simulation to see how sparse variables change with the system imperfection. Exemplar estimates of wave gradient and trajectory in k-space are presented in Supporting Information Figure S2.

3.3 | Wave-EPI reconstruction

We reconstructed single-shot wave-EPI data using dual wave-PSFs and coil sensitivity maps calibrated from additional reference scans as follows.

$$I = \underset{I}{\mathrm{argmin}} \left\| \begin{bmatrix} W_p \mathcal{F}_y P(\varrho_p) \\ W_n \mathcal{F}_y P(\varrho_n) \end{bmatrix} \mathcal{F}_x CI - \begin{bmatrix} S_p \\ S_n \end{bmatrix} \right\|_2^2 \quad (8)$$

where I is the unknown image, p denotes the positive lines, n denotes the negative lines, C is the coil-sensitivity map, and S_p and S_n are the acquired wave-EPI k-space signal from the positive and negative readouts, respectively. We extend the single-shot reconstruction to multi-shot wave-EPI by exploiting low-rankness across multiple shots

using the MUSSELS approach.[18] Wave-EPI reconstruction with Hankel low-rank constraint between multiple shots is described as follows.

$$I = \underset{I}{\arg\min} \sum_s \left\| \begin{bmatrix} W_p \mathcal{F}_y P\left(\varrho_p\right) \\ W_n \mathcal{F}_y P\left(\varrho_n\right) \end{bmatrix} \mathcal{F}_x C I_s - \begin{bmatrix} S_{s,p} \\ S_{s,n} \end{bmatrix} \right\|_2^2 + \|\mathcal{H}(I)\|_* \qquad (9)$$

where I_s is the reconstructed image of the s-th shot, $\mathcal{H}$ is the Hankel matrix, and $\| \cdot \|_*$ represents nuclear norm constraints, respectively. We exploit fast iterative shrinkage-thresholding algorithm (FISTA[46]) to make the loss function more stable. To minimize the nuclear norm constraints, we used the SVD-based thresholding approach.[19,21] Exemplar code and data can be found at "https://github.com/jaejin-cho/wave-EPI".

3.4 | Joint image reconstruction for wave-EPI with g-Slider RF-encoding

Wave-EPI is also able to take advantage of the g-Slider approach, which provides SNR gain by performing multiple RF encoded acquisitions over a thin slab to resolve information from multiple slices.[43] However, Equation (9) may induce a non-negligible voxel blurring due to increased intra-voxel phase variation within a relatively thick, e.g., 5 mm, slab. We use wave-PSFs at the thin-slice resolution to combat this, and directly estimate the thin-slice resolution images. Exemplar wave PSFs are shown in Supporting Information Figure S3. We propose a joint image reconstruction method to take advantage of g-Slider's SNR gain while minimizing voxel blurring caused by wave-encoding. We estimate shot-to-shot phase variations from the reconstructed interim RF-encoded and multi-shot images using the Equation (9) in advance and use this information during the joint reconstruction. This joint reconstruction using the pre-estimated shot-to-shot phase information for wave-EPI with g-Slider RF-encoding to reconstruct the thin-slice image I_h can be described as follows.

$$I_h = \underset{I_h}{\arg\min} \sum_s \sum_g \times \left\| \begin{bmatrix} W_p \mathcal{F}_y G_r P\left(\varrho_p\right) \\ W_n \mathcal{F}_y G_r P\left(\varrho_n\right) \end{bmatrix} \mathcal{F}_x C \Phi_{s,r} I_h - \begin{bmatrix} S_{s,r,p} \\ S_{s,r,n} \end{bmatrix} \right\|_2^2 \qquad (10)$$

where r denotes g-Slider RF encoding index, G_r is the RF encoding matrix, $\Phi_{s,r}$ is the estimated shot-to-shot phase variation in shot s, RF index r, and $S_{s,r,p}$ and $S_{s,r,n}$ are the acquired s-th shot, r-th RF encoding signal from positive and negative readouts, respectively.

To provide an initial guess to the optimizer, we directly applied G_r^{-1} to the phase-removed interim shot images.

3.5 | Data acquisition

Three different in-vivo experiments highlighting the versatility of wave-EPI were conducted with the approval of the Institutional Review Board (IRB) using a 3T Siemens Prisma system and a 32-channel head coil. Table 1 shows the imaging parameters used for the in-vivo experiments; single-shot GE-EPI at two different reduction factors, two-shot SE-EPI for dMRI, and two-shot SE-EPI with g-Slider for dMRI.[43] For MS-EPI, we present the reduction factor per single EPI shot ($R_{shot} = R_{in} \times R_{sms}$). Blipped-CAIPI was used for comparison in all experiments. Coil sensitivity maps were calculated from pre-acquired low-resolution FLASH scans using ESPIRiT.[13,47] For dMRI, we used 1000s/mm^2 of b-value and used Hankel structured low-rank regularization with 7×7 kernels to mitigate shot-to-shot phase variations. We kept 37.5% of singular values during the SVD-truncation for the low-rank regularization, where we estimated the truncation level by maximizing the second fiber population count as shown in Supporting Information Figure S4.[48,49] We used the Marchenko-Pastur (MP-) PCA denoising algorithm as implemented in the MRTRIX toolbox to further denoise the reconstructed images[50,51] and FSL diffusion toolbox using tract-based spatial statistics for diffusion processing.[52] Five different RF pulses were used for g-Slider acquisition to encode thin-slice information, which resolve a 5-mm slab into five 1-mm slices.[43] For GE-EPI and SE-EPI experiments at 1.25 mm isotropic resolution, we were able to achieve the maximum wave amount constrained by hardware slew rate limitation. However, for dMRI with g-Slider experiments, we could use only wave gradients of 22mT/m × 19mT/m due to PNS limits, where the maximum wave gradient constrained by the slew rate would have been 40mT/m × 20mT/m.

4 | RESULTS

4.1 | Single-shot GE-EPI

Figure 3 shows 1.25 mm isotropic whole-brain single-shot GE-EPI images at $R_{in} \times R_{sms} = 3 \times 3$. As pointed out by the red arrows in Figure 3, blipped-CAIPI suffers from reconstruction artifacts due to high acceleration, which were mitigated by wave-encoding. Based on the g-factor analysis, wave-EPI reduced average and maximum g-factors by

TABLE 1 Imaging parameters for in-vivo experiments

	GE-EPI				dMRI SE-EPI		dMRI g-Slider			
	Figure 3		Figure S5		Figures 4, 5, S6		Figures 6, 7, S4		Figure S7	
	Blipped-CAIPI	Wave-EPI	Blipped-CAIPI	Wave-EPI	Blipped-CAIPI	Wave-EPI	Blipped-CAIPI	Wave-EPI	Blipped-CAIPI	Wave-EPI
Imaging plane	Axial	Axial	Axial	Axial	Axial	Axial	Axial	Axial	Axial	Axial
FOV [mm^3]	220×220×132		220×220×132		220×220×130		220×216×150		220×220×150	
Resolution [mm^3]	1.25×1.25×1.25		1.25×1.25×1.25		1.25×1.25×1.25		1.00×1.00×1.00		1.00×1.00×1.00	
TR [ms]	2800		2400		6900		3000		3000	
TE [ms]	27	28	23	24	73	73	70	71	72	73
Readout gradient [mT/m]	31.42		31.42		31.42		35.59		35.59	
Wave-gradient [mT/m]^2	-	29×15	-	29×15	-	30×15	-	22×19	-	21×16
Maximum slope in k-space	-	0.92×0.48	-	0.92×0.48	-	0.95×0.48	-	0.62×0.53	-	0.59×0.45
# of shots	1		1		2		2		1	
Reduction factor per each shot ($R_{shot} = R_{in} \times R_{sms}$)	3×3		4×3		5×2		6×2		3×2	
Receiver bandwidth [Hz/pixel]	1672		1672		1672		1516		1516	
Partial Fourier factor	6/8		6/8		6/8		8/8		6/8	
b-value [s/mm^2]	-		-		1000		1000		1000	
# of diffusion directions	-		-		32		63		20	
# of b0 acquisition	-		-		4		8		1	
# of RFs for g-Slider encoding	-		-		-		5		5	
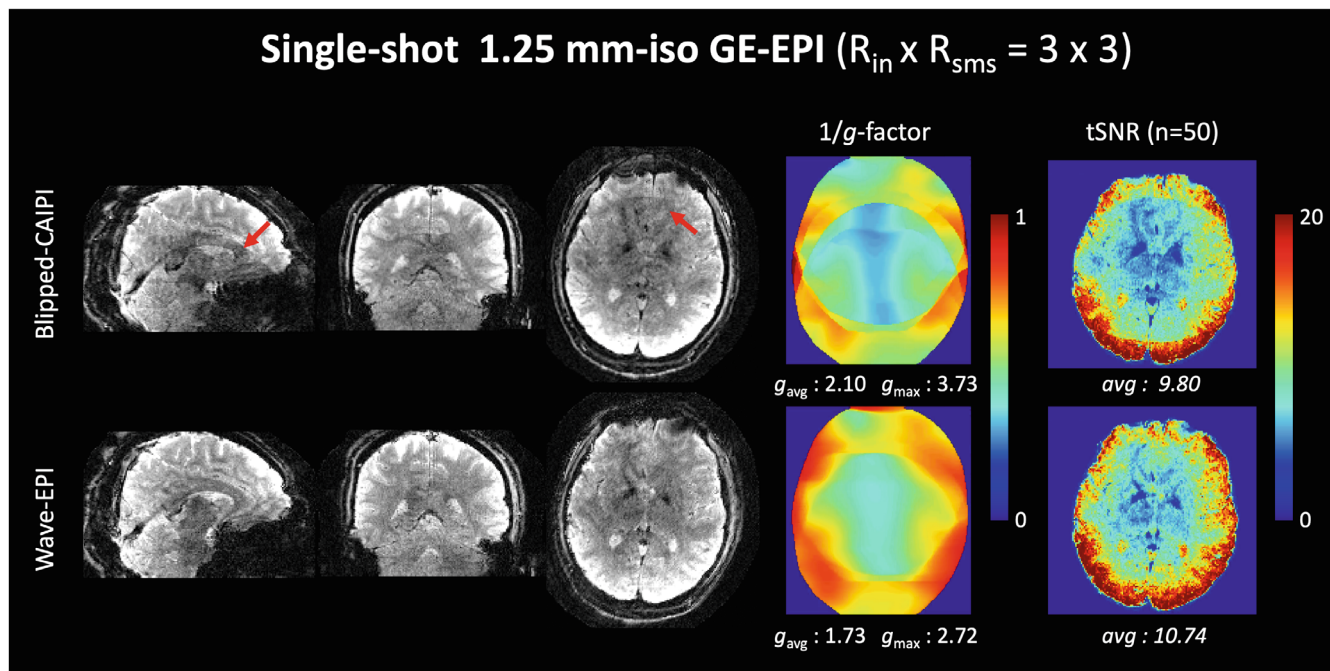
FIGURE 3 The reconstructed images, g-factor analysis, and tSNR maps of single-shot GE-EPI at $R_{in} \times R_{sms} = 3 \times 3$
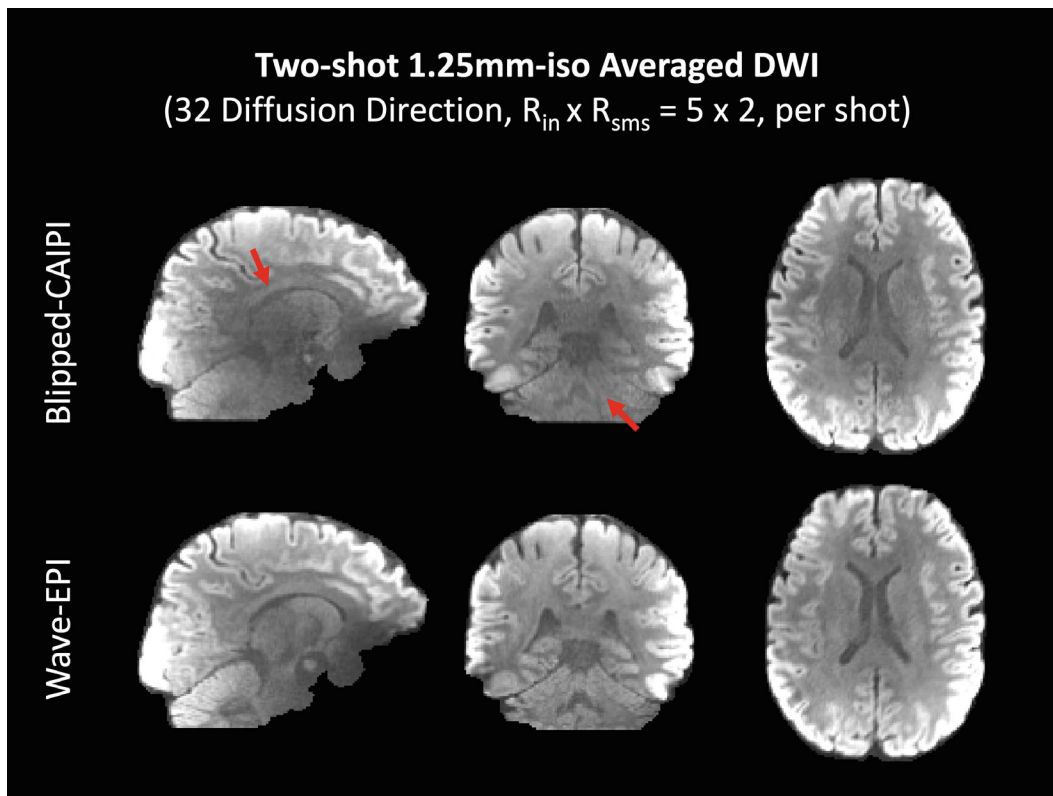
FIGURE 4 The 32 diffusion-direction DWI with 1000s/mm^2 of b-value using the two-shot SE-EPI at $R_{in} \times R_{sms} = 5 \times 2$ per each EPI-shot

1.21- and 1.37-fold compared to standard blipped-CAIPI in the center slice, respectively. Temproal SNR (tSNR) maps were also calculated from a time-series comprising 50 TRs to quantify the tSNR gain of wave-EPI over blipped-CAIPI.

Wave-EPI increased the averaged tSNR by 9.6% compared to standard blipped-CAIPI.

We further pushed the reduction factor to $R_{in} \times R_{sms} = 4 \times 3$ as shown in Supporting Information

Figure S5. Wave-EPI significantly mitigated the aliasing artifact and noise amplification for this highly accelerated scan. In the g-factor analysis, wave-EPI reduced average and maximum g-factors by 1.41- and 1.77-fold compared to the standard blipped-CAIPI and tSNR maps also show 5.6% of the averaged tSNR gain by wave-EPI.

4.2 | Two-shot SE-EPI for dMRI

Figures 4 and 5 show average DWI images and fractional anisotropy (FA) map color-encoded by the primary eigenvector at b = 1000s/mm^2 with 32 directions at 1.25 mm isotropic voxel size using two-shot SE-EPI with $R_{in} \times R_{sms} = 5 \times 2$ per shot. Wave-CAIPI was able to substantially reduce artifacts and noise amplification over blipped-CAIPI despite the high acceleration level. Supporting Information Figure S6 shows the DWI of a single diffusion direction, which demonstrates the large noise and aliasing reductions in wave-EPI.

4.3 | Two-shot SE-EPI with g-Slider for dMRI

Figures 6 and 7 show the average DWI images and colored FA map at b = 1000s/mm^2 for 63-direction data at 1 mm isotropic voxel size using two-shot SE-EPI with $R_{in} \times R_{sms} = 6 \times 2$ per shot. Blipped-CAIPI with g-Slider suffers from reduced SNR and stripe artifacts in both DWI and FA images. In Figure 6, the red arrows point to the remaining aliasing artifacts in blipped-CAIPI. Standard wave-EPI with g-Slider was able to largely mitigate both aliasing and striping artifacts, and joint reconstruction of wave-EPI and g-Slider further removed the striping artifact. In Figure 7, wave-EPI significantly improves the FA map and reduces noise. In the region of interest (ROI) in the solid-line box in the axial view, wave-EPI clearly visualizes sub-cortical white matter fascicles coherently fanning into the cortex and the orthogonality between the primary fiber orientations in the cerebral cortex and the cortical surface while blipped-CAIPI has difficulty representing the orthogonality. In the ROI in the dashed-line box in the axial view, wave-EPI displays in exquisite detail the gray matter bridges that span the internal capsule, giving rise to the characteristic stripes seen in the striatum. We observed the significant improvement of wave-EPI in the coronal and sagittal views as well.

5 | DISCUSSION

We introduced wave-EPI, which extended wave encoding to EPI acquisition and incorporated inter-slice shifts,
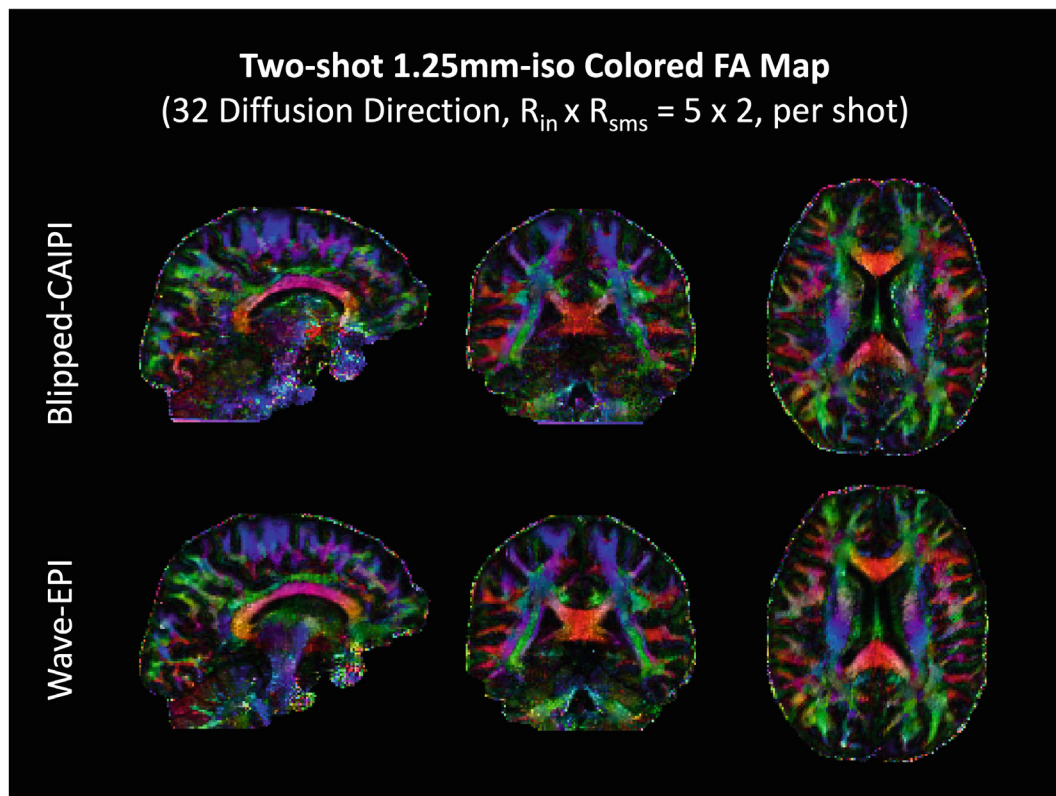
FIGURE 5 The 32 diffusion-direction colored FA maps with 1000s/mm^2 of b-value using the two-shot SE-EPI at $R_{in} \times R_{sms} = 5 \times 2$ per each EPI-shot

FIGURE 6 The 63 diffusion-direction DWI with 1000s/mm^2 of b-value using the two-shot SE-EPI at $R_{in} \times R_{sms} = 6 \times 2$ per each EPI-shot. Five different encoded RFs were used for high-resolution g-Slider. We reconstructed wave-EPI images using standard wave-EPI reconstruction before g-Slider decoding and joint reconstruction of wave-EPI and g-Slider
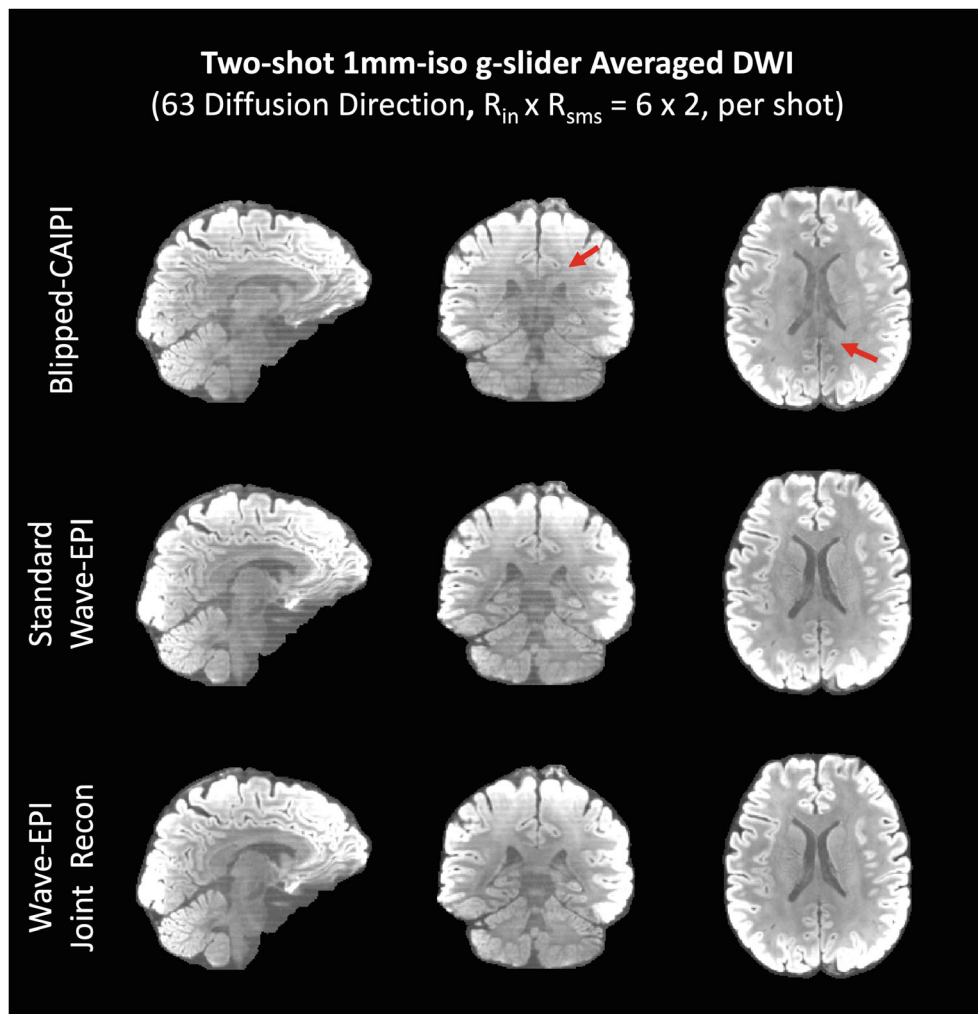
and for multi-shot acquisitions, structured low-rank regularization for navigator-free reconstruction. This extreme controlled aliasing approach was able to substantially reduce g-factor noise amplification and aliasing artifacts over standard blipped-CAIPI for a range of image contrasts at high acceleration rates, with either single- or multi-shot acquisition.

Using estimated dual PSFs instead of the theoretical waveforms provided robustness against gradient imperfections in the wave-EPI reconstruction. Our FLEET-based calibration acquisitions for PSF estimation require ~1 min of additional scan time for a 30-slab g-Slider acquisition. Diffusion and functional imaging experiments often entail the acquisition of a large number of TRs for dense sampling of q-space in dMRI, and for characterization of the hemodynamic response in fMRI. Since these acquisitions usually last several minutes, we anticipate that the additional ~1 min of calibration will not impact their feasibility significantly. Standard blipped-CAIPI acquisitions lend themselves to GRAPPA/slice-GRAPPA based reconstructions, which also entail additional calibration scans with

FLEET ordering and require similar amounts of added acquisition time. Through our generalized-SENSE reconstruction in wave-EPI, we obviated the need for these kernel calibration acquisitions and estimated coil sensitivities from a fast, ~11 s FLASH scan for 30 slices. To calibrate the y and z wave-PSFs, the projected signal along the z and y axes (k_x-z image and k_x-y image) can be used, respectively.[53] By using the projected signal, the additional scan time can be theoretically reduced to ~7 s.

Relatively low readout bandwidths in spin-warp applications of wave encoding allow for near-perfect g-factor performance at, e.g., R = 3×3 acceleration using a 32 channel head coil.[31,32] The much shorter readout window in EPI acquisition precluded our ability to achieve similar g-factor performance. As detailed in the Theory section, a shorter readout window decreases the voxel spreading. In addition, maximum wave gradient is limited by hardware slew rate limitation and peripheral nerve stimulation. To combat this issue, we proposed to use a "half-cycle" cosine waveform to achieve a larger gradient amplitude and voxel spreading effect while satisfying the
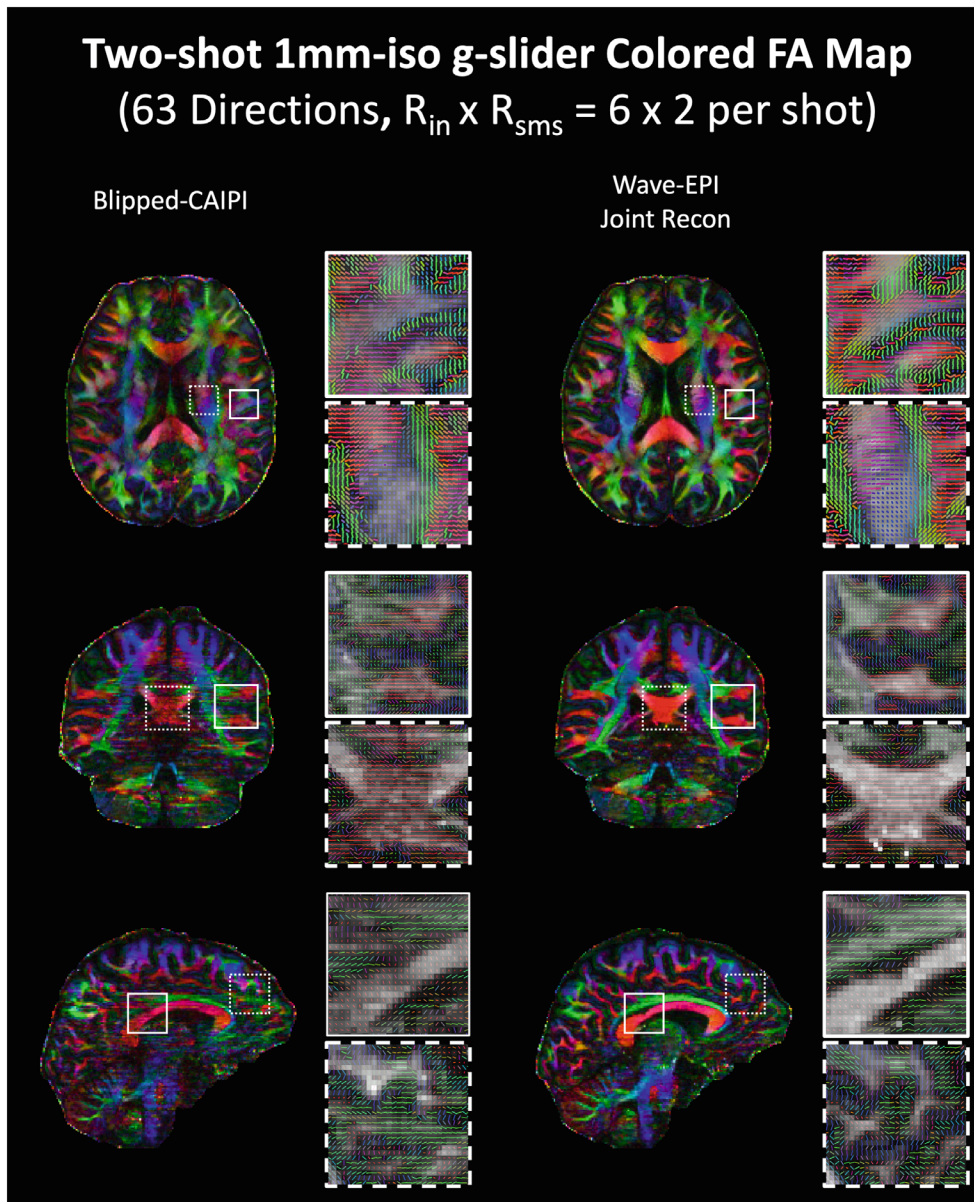
FIGURE 7 The 63 diffusion-direction colored FA maps with 1000s/mm^2 of b-value using the two-shot SE-EPI at $R_{in} \times R_{sms} = 6 \times 2$ per each EPI-shot. Five different encoded RFs were used for high-resolution g-Slider

slew rate and stimulation constraints. We simulated the voxel spreading for half- and one-cycle waveforms with the same maximum slew rate, at 1.25 mm isotropic resolution with $R_{in} \times R_{sms} = 4 \times 3$ as shown in Figure 8. One- and half-cycle cosine wave-gradients had 15mT/m and 30mT/m amplitudes in the phase-encoding direction, respectively. 15mT/m of one-cycle sine wave-gradient was applied in the slice-selection direction in both cases. Relative to one-cycle cosine wave, half-cycle cosine yielded more spreading in the image domain, which led to reduced g-factor penalty. Compared to blipped-CAIPI, wave encoding with one-cycle cosine reduced the average g-factor by 1.10-fold. With the half-cycle approach, the average g-factor gain was 1.23-fold. The g-factor gain with the half-cycle approach implies that wave-EPI provides a mean SNR benefit of ∼1.5-averages of blipped-CAIPI

acquisition at no cost in acquisition time at 1.25 mm isotropic resolution with $R_{in} \times R_{sms} = 4 \times 3$. In addition, the relative stimulation levels for one TR at a 3T Siemens Prisma scanner were computed by the MR IDEA VE11C software as shown in Figure 8. The half-cycle cosine wave remained within PNS safety limits and provided more g-factor gain compared to the one-cycle cosine wave, which could not be played on the scanner as it exceeded stimulation limits. One-cycle of cosine wave starts and ends its gradient at the highest points, which might increase the ramp-up and -down time due to the slew rate and stimulation limitations. On the other hand, half-cycle cosine encoding starts and ends its gradient at zero amplitude and saves its slew rate and stimulation during the ramp-up and -down time.
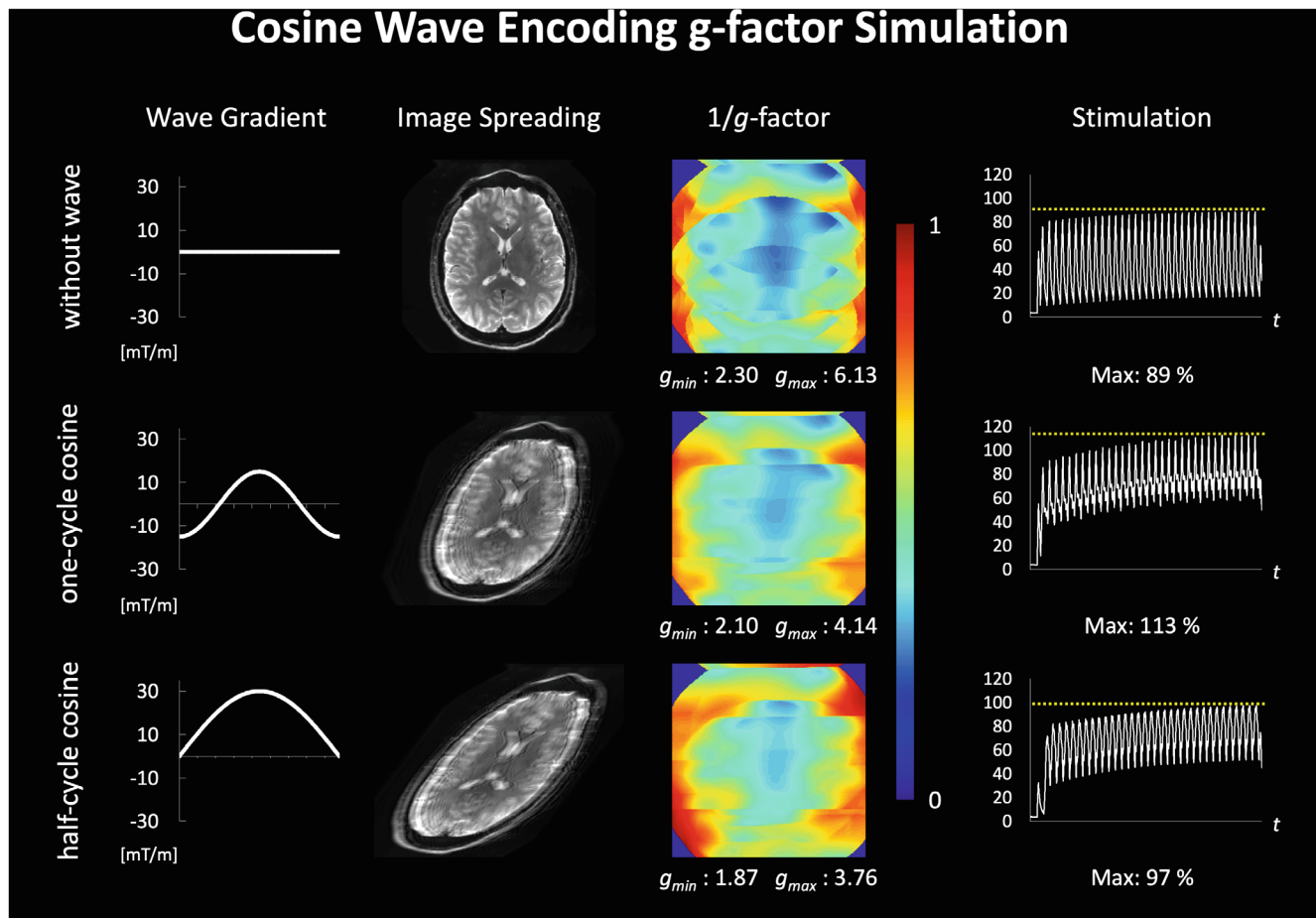
FIGURE 8   Signal spreading simulation at 1.25 mm isotropy voxel size with $R_{in} \times R_{sms} = 4 \times 3$. One- and half-cycle cosine wave-gradients had 15 mT/m and 30 mT/m amplitudes in the phase-encoding direction, respectively, and 15 mT/m of one-cycle sine wave-gradient was applied in the slice-selection direction in both cases. The stimulation levels for one TR were shown in the last column, which were computed by SIEMENS IDEA software for pulse sequence programming

In our current acquisitions, we have only sampled data during the "flat-top" portion of the EPI readout. Using ramp sampling would further increase the acquisition efficiency and decrease the echo spacing. Our simulations indicate that the echo spacing can be reduced by ~10% at 1 mm resolution. Our observations suggest that the proposed PSF calibration scan is flexible enough to allow for incorporating ramp sampling for this additional efficiency gain. Another minor drawback of wave encoding is the fact that the pre-phasing lobe of sinusoidal gradient waveform increases the minimum TE by about 1 ms. Assuming a typical T_2 value of 60 ms, this would reduce the SNR level in dMRI by ~2%. This difference, however, is easily offset by wave-EPI's ability to provide higher in-plane acceleration. Currently, the amount of wave-encoding is limited by PNS dominantly. At 1 mm resolution imaging, we could only achieve the 22 mT/m of maximum wave gradient in the phase-encoding direction at 1 mm resolution because of PNS, where the maximum gradient constrained by

the slew rate is 38 mT/m. We anticipate that advanced hardware systems with higher slew and relaxed nerve stimulation limits (e.g., with head-insert or head-only gradients) will allow for yet higher acceleration by enabling the use of larger wave gradient amplitudes.

At 1 mm isotropic resolution and $R_{in} \times R_{sms} = 6 \times 2$ per shot, effective echo spacing time was 173 us. This represents 26.27 Hz in the k_y direction at 220 mm FOV, which leads to maximum 1.91 mm shift in the y direction with a 50 Hz field map variation. Although the wave encoding is applied linearly in the spatial domain, geometric distortions can cause inaccurate wave PSF information to be used during reconstruction thereby inducing minor blurring in the readout direction. We mitigated Nyquist ghost artifacts using four different wave PSFs, reflecting the gradient time delays and phase difference between positive and negative wave gradients, in addition to traditional navigators for readout gradients. Despite a short echo spacing time at a high reduction factor, signal decay due to T_2 and T_2^* effects along with phase encoding still leads to the

blurring in the k_y direction regardless of wave-encoding. In addition, unacquired k-space due to partial Fourier causes the blurring in the k_y direction. These effects can be in part mitigated with the virtual coil approach and Hankel low-rank constraint.

For g-Slider encoding, five RFs were used to resolve a 5-mm slice into five 1-mm slices. We estimated and removed the shot-to-shot variations for g-Slider, but inaccurate phase estimations due to the high acceleration might have worsened the conditioning of the g-Slider forward model as shown in the blipped-CAIPI images in Figure 6. Supporting Information Figure S7 shows average DWI images using single-shot SE-EPI with g-Slider RF encoding at the lower acceleration rate of $R_{in} \times R_{sms} = 3 \times 2$, where both blipped-CAIPI and wave-EPI provided clean reconstructions. At this lower acceleration rate, both blipped-CAIPI and wave-EPI were able to estimate the phase of each RF encode accurately, enabling successful self-navigation of phase differences in g-Slider reconstruction. On the other hand, the proposed joint reconstruction could be further improved by incorporating B1 inhomogeneity and T1 relaxation considerations into g-Slider RF encoding calculation to further mitigate any remaining striping artifacts in wave-EPI even at high accelerations. The current joint reconstruction model uses a 5×5 matrix, which does not consider the contribution from the adjacent slabs to the target slab's magnetization.

The voxel spreading effect of wave gradients is continuous across space and, thus, has the potential to cause within-voxel blurring since the top and bottom edges of each voxel will experience slightly different PSFs. We simulated the amount of this within-voxel blurring at $1 \times 1 \times 1$ mm^3 resolution in Figure 9. As shown in Figure 9C, standard wave-EPI extended FWHM by 0.01 mm and generated 8% of sidelobes due to the 5 mm thick slab before g-Slider reconstruction. The remaining intravoxel phase variation also contributes to the stripe artifacts observed in Figure 6. Meanwhile, joint reconstruction of wave-EPI and g-Slider only extended FWHM by 0.01 mm and reduced intra-voxel blurring to negligible levels. We further investigated the intra-voxel blurring for larger amounts of wave-encoding gradients at an advanced 7 T hardware system with head gradient coil[54] in Supporting Information Figure S8.

Wave-encoding can improve the image reconstruction condition by acquiring the points in the missing k-space lines. An exemplar and related "zig-zag" trajectory is shown in Supporting Information Figure S9a. The readout trajectory shifts up and back by Δk_y for every sampling point at reduction factor R = 2. Because of the oversampling in the x direction, the trajectory can cover all missing lines without affecting scan time while avoiding folding artifacts along the readout axis. This sampling pattern reduces the effective reduction factor in the k_y direction up to two-fold theoretically. However, this sampling pattern is not possible with current gradient systems as well as due to PNS constraints. Zigzag GRAPPA[55] and wave-CAIPI[31,32] are practical implementations that acquire k-space points in the missing lines to reduce the effective reduction in the k_y direction with the current hardware systems, while respecting PNS constraints. Supporting Information Figure S9b shows practical implementation with wave-encoded trajectory.

The proposed half-cycle cosine wave encoding also acquires k-space points in the missing lines to improve the reconstruction condition by reducing the effective reduction factor in the k_y direction. With respect to the acquisition with the oblique straight readouts as in view angle tilting (VAT),[56,57] half-cycle cosine wave encoding has the same trajectory slope at the center of k-space. However, the slope of half-cycle wave encoding is continuously changing along the k_x direction, and the slope becomes zero at the edge of the k-space, as in Cartesian sampling. As a result, the half-cycle wave encoding takes an advantage of tilted trajectory, acquiring k-space points in the missing lines and reducing the effective reduction in the k_y direction, while minimizing the blurring by continuously changing slope along the k_x direction, as shown in Supporting Information Figure S10. By achieving 1 cycle with retaining the same G_w with an advanced hardware system, the resolution loss can decrease to 0.03% and become negligible, while preserving g-factor benefits. In the k_x-k_z domain, one-cycle sine wave encoding has zero slope at both edge and center of k-space, and maximum slopes are placed at $\frac{1}{4}$ and $\frac{3}{4}$ points of the readout. At 1.25 mm, 15 mT/m of sine encoding has no resolution loss.

We scanned a resolution phantom to investigate the effect in the image resolution by half-cycle cosine wave-encoding gradients, as shown in the Supporting Information Figure S11. We applied 29 mT/m of cosine gradient in the phase-encoding direction. In the simulation, we expected a 3% increase in FWHM, and observed comparable image resolution based on the detailed structures in the phantom as expected from the PSF simulation. We theoretically explained the phase inducing the resolution loss in Supporting Information Script.

The wave-encoding improves the image reconstruction condition using the coil sensitivity variations in the x direction. The bigger spreading can use the bigger coil sensitivity difference and improve the image restoration condition more efficiently. As shown in Equation (4), the maximum

FIGURE 9 Intra-voxel dephasing simulation at 1 mm isotropy voxel size. 22 mT/m × 19 mT/m of wave-encoding were applied. A, The phase variation within a voxel. B, Wave gradients and corresponding spatial frequencies during a readout. C, PSF simulations using the standard wave-EPI reconstruction and joint reconstruction of wave-EPI and g-Slider
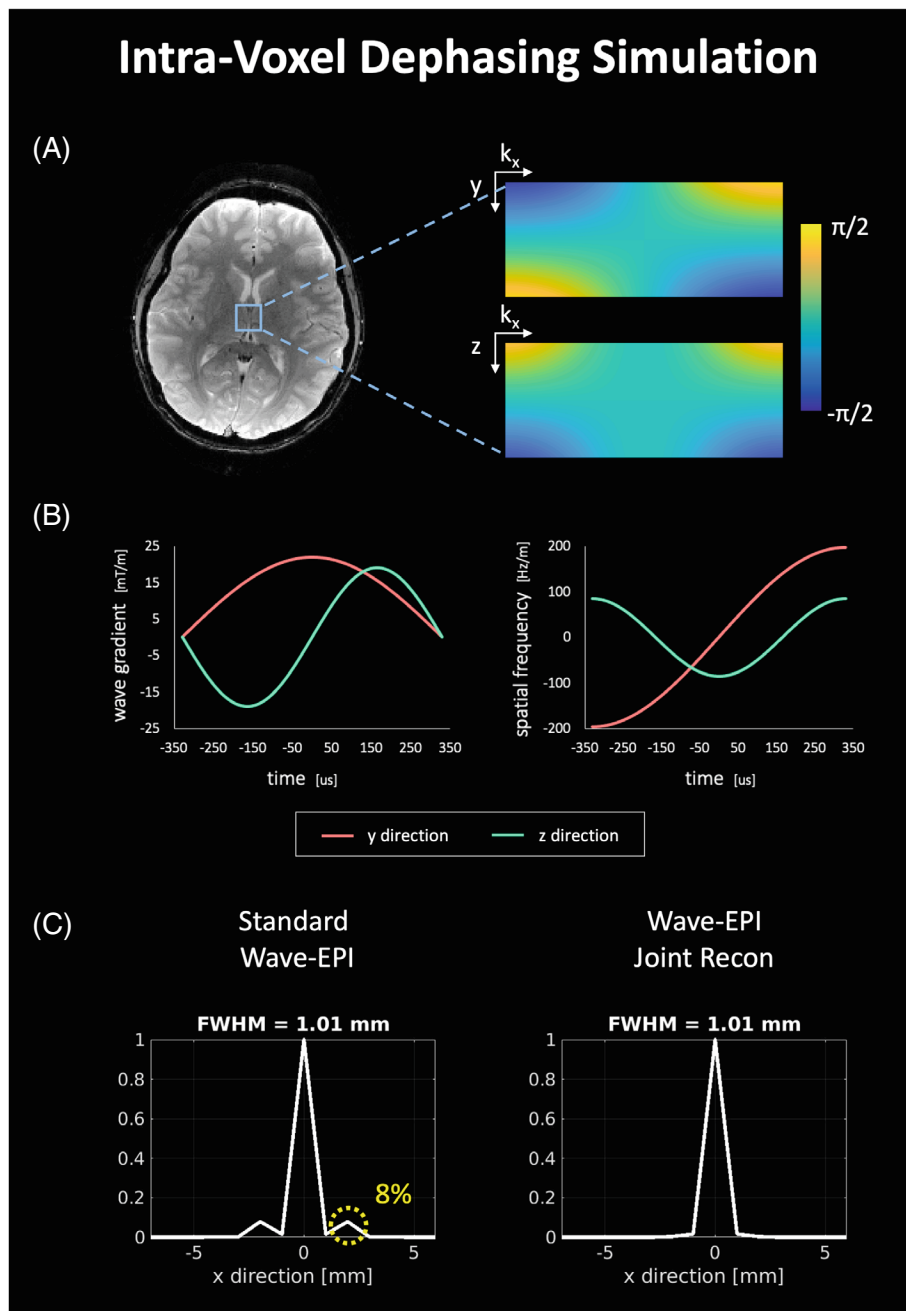
image spreading distance is defined as $\frac{y}{2\pi} \cdot \frac{G_w}{G_x}$. In k-space, we can intuitively guess the conditioning improvement by wave-encoding using the maximum slope of the trajectory, $\frac{G_w}{G_x}$, in the k_x-k_y and k_x-k_z domains.

Wave-EPI reconstruction for single-shot acquisition requires 29 s per slice-group, whereas this is 28 s/slice-group in blipped-CAIPI. The additional low-rank thresholding step in multi-shot acquisition further increases the reconstruction time to 3.8 min/slice-group for wave- and 3.2 min/slice-group in blipped-CAIPI. Our current Matlab implementation makes use of parallel processing across the slice groups,

but further speed-up is possible through additional parallelization across volumes, code optimization, and alternate reconstruction algorithms such as unrolled networks,[58–61] which can learn more efficient ways to perform gradient descent along with learned regularizers.

6 | CONCLUSIONS

Wave-CAIPI was proposed to enable combined and high in-plane and SMS acceleration factors to improve the geometric fidelity and acquisition speed of EPI. Its

application was demonstrated in GE, SE, and diffusion contrasts with single- and multi-shot acquisition, and g-Slider RF encoding was incorporated for high isotropic resolution imaging. Dual wave-PSFs and structured low-rank regularization were introduced to improve the robustness of its reconstruction to trajectory errors and shot-to-shot variations. We proposed a joint image reconstruction method for wave-EPI with g-Slider to minimize the intra-voxel blurring by wave-encoding. In-vivo experiments showed that wave-EPI acquisition allows high acceleration rates with decreased g-factor penalty and image artifacts relative to blipped-CAIPI EPI.

CONFLICT OF INTERESTS
Wei-Ching Lo is an employee in Siemens Medical Solutions.

ORCID
Jaejin Cho https://orcid.org/0000-0001-5672-6765
Congyu Liao https://orcid.org/0000-0003-2270-276X
Qiyuan Tian https://orcid.org/0000-0002-8350-5295
Zijing Zhang https://orcid.org/0000-0002-3354-7948
Benedikt A. Poser https://orcid.org/0000-0001-8190-4367
Jason Stockmann https://orcid.org/0000-0001-8454-5347
Berkin Bilgic https://orcid.org/0000-0002-9080-7865

REFERENCES
1. Mansfield P. Multi-planar image formation using NMR spin echoes. *J Phys C*. 1977;10:L55-L58.
2. Stehling MK, Turner R, Mansfield P. Echo-planar imaging: magnetic resonance imaging in a fraction of a second. *Science*. 1991;254:43-50.
3. Poustchi-Amin M, Mirowitz SA, Brown JJ, McKinstry RC, Li T. Principles and applications of echo-planar imaging: a review for the general radiologist. *Radiographics*. 2001; 21:767-779.
4. Deichmann R, Gottfried JA, Hutton C, Turner R. Optimized EPI for fMRI studies of the orbitofrontal cortex. *Neuroimage*. 2003;19:430-441.
5. Bammer R, Auer M, Keeling SL, et al. Diffusion tensor imaging using single-shot SENSE-EPI. *Magn Reson Med*. 2002;48:128-136.
6. Andersson JL, Skare S. Image distortion and its correction in diffusion MRI. *Diffusion MRI: Theory, Methods, and Applications*; Oxford University Press; 2010:285-302.
7. Jezzard P, Balaban RS. Correction for geometric distortion in echo planar images from B0 field variations. *Magn Reson Med*. 1995;34:65-73.
8. Griswold MA, Jakob PM & Heidemann RM et al. Off-resonance artifacts in single shot EPI using partially parallel imaging. 446. 2001.
9. Heidemann RM, Griswold MA & Porter D et al. Minimizing distortions and blurring in diffusion weighted single shot EPI using high performance gradients in combination with parallel imaging. In: Proceedings of the 9th Annual Meeting of the ISMRM. Vol. 169. 2001.
10. Bammer R, Keeling SL, Augustin M, et al. Improved diffusion-weighted single-shot echo-planar imaging (EPI) in stroke using sensitivity encoding (SENSE). *Magn Reson Med*. 2001;46:548-554.
11. Griswold MA, Jakob PM, Heidemann RM, et al. Generalized autocalibrating partially parallel acquisitions (GRAPPA). *Magn Reson Med*. 2002;47:1202-1210.
12. Pruessmann KP, Weiger M, Scheidegger MB, Boesiger P. SENSE: sensitivity encoding for fast MRI. *Magn Reson Med*. 1999;42:952-962.
13. Uecker M, Lai P, Murphy MJ, et al. ESPIRiT—an eigenvalue approach to autocalibrating parallel MRI: where SENSE meets GRAPPA. *Magn Reson Med*. 2014;71:990-1001.
14. Ordidge RJ, Helpern JA, Qing ZX, Knight RA, Nagesh V. Correction of motional artifacts in diffusion-weighted MR images using navigator echoes. *Magn Reson Imaging*. 1994;12:455-460.
15. Butts K, Pauly J, De Crespigny A, Moseley M. Isotropic diffusion-weighted and spiral-navigated interleaved EPI for routine imaging of acute stroke. *Magn Reson Med*. 1997;38:741-749.
16. Miller KL, Pauly JM. Nonlinear phase correction for navigated diffusion imaging. *Magn Reson Med*. 2003;50:343-353.
17. Chen N, Guidon A, Chang H-C, Song AW. A robust multi-shot scan strategy for high-resolution diffusion weighted MRI enabled by multiplexed sensitivity-encoding (MUSE). *Neuroimage*. 2013;72:41-47.
18. Mani M, Jacob M, Kelley D, Magnotta V. Multi-shot sensitivity-encoded diffusion data recovery using structured low-rank matrix completion (MUSSELS): annihilating filter K-space formulation for multi-shot DWI recovery. *Magn Reson Med*. 2017;78:494-507.
19. Haldar JP. Low-Rank Modeling of Local k-Space Neighborhoods (LORAKS) for Constrained MRI. *IEEE Trans Med Imaging*. 2014;33:668-681.
20. Haldar JP, Zhuo J. P-LORAKS: low-rank modeling of local k-space neighborhoods with parallel imaging data. *Magn Reson Med*. 2016;75:1499-1514.
21. Shin PJ, Larson PE, Ohliger MA, et al. Calibrationless parallel imaging reconstruction based on structured low-rank matrix completion. *Magn Reson Med*. 2014;72:959-970.
22. Jin KH, Lee D, Ye JC. A General Framework for Compressed Sensing and Parallel MRI Using Annihilating Filter Based Low-Rank Hankel Matrix. *IEEE Trans Comput Imaging*. 2016;2:480-495.
23. Lee J, Jin KH, Ye JC. Reference-free single-pass EPI Nyquist ghost correction using annihilating filter-based low rank Hankel matrix (ALOHA). *Magn Reson Med*. 2016;76:1775-1789.

24. Lobos RA, Kim TH, Hoge WS, Haldar JP. Navigator-free EPI ghost correction with structured low-rank matrix models: new theory and methods. *IEEE Trans Med Imaging*. 2018;37:2390-2402.

25. Larkman DJ, Hajnal JV, Herlihy AH, Coutts GA, Young IR, Ehnholm G. Use of multicoil arrays for separation of signal from multiple slices simultaneously excited. *J Magn Reson Imaging*. 2001;13:313-317.

26. Nunes RG, Hajnal JV, Golay X, Larkman DJ. Simultaneous slice excitation and reconstruction for single shot EPI. *Proc Intl Soc Mag Reson Med*. 2006;14:293.

27. Moeller S, Yacoub E, Olman CA, et al. Multiband multislice GE-EPI at 7 tesla, with 16-fold acceleration using partial parallel imaging with application to high spatial and temporal whole-brain fMRI. *Magn Reson Med*. 2010;63:1144-1153.

28. Feinberg DA, Moeller S, Smith SM, et al. Multiplexed Echo planar imaging for sub-second whole brain FMRI and fast diffusion imaging. *PLoS One*. 2010;5:e15710.

29. Breuer FA, Blaimer M, Heidemann RM, Mueller MF, Griswold MA, Jakob PM. Controlled aliasing in parallel imaging results in higher acceleration (CAIPIRINHA) for multi-slice imaging. *Magn Reson Med*. 2005;53:684-691.

30. Setsompop K, Gagoski BA, Polimeni JR, Witzel T, Wedeen VJ, Wald LL. Blipped-controlled aliasing in parallel imaging for simultaneous multislice echo planar imaging with reduced g-factor penalty. *Magn Reson Med*. 2012;67:1210-1224.

31. Bilgic B, Gagoski BA, Cauley SF, et al. Wave-CAIPI for highly accelerated 3D imaging. *Magn Reson Med*. 2015;73:2152-2162.

32. Gagoski BA, Bilgic B, Eichner C, et al. RARE/turbo spin echo imaging with simultaneous multislice wave-CAIPI: RARE/TSE with SMS wave-CAIPI. *Magn Reson Med*. 2015;73:929-938.

33. Breuer FA, Blaimer M, Mueller MF, et al. Controlled aliasing in volumetric parallel imaging (2D CAIPIRINHA). *Magn Reson Med*. 2006;55:549-556.

34. Polak D, Setsompop K, Cauley SF, et al. Wave-CAIPI for highly accelerated MP-RAGE imaging. *Magn Reson Med*. 2018;79:401-406.

35. Schwarz JM, Pracht ED, Brenner D, Reuter M, Stöcker T. GRAPPA reconstructed wave-CAIPI MP-RAGE at 7 tesla. *Magn Reson Med*. 2018;80:2427-2438.

36. Kim TH, Bilgic B, Polak D, Setsompop K, Haldar JP. Wave-LORAKS: combining wave encoding with structured low-rank matrix modeling for more highly accelerated 3D imaging. *Magn Reson Med*. 2019;81:1620-1633.

37. Chen F, Taviani V, Tamir JI, et al. Self-calibrating wave-encoded variable-density single-shot fast spin echo imaging. *J Magn Reson Imaging*. 2018;47:954-966.

38. Poser BA, Bilgic B, Gagoski BA, et al. Echo-planar imaging with wave-CAIPI acquisition and reconstruction. In: Proceedings of the 25th Scientific Meeting of ISMRM. Honolulu; 2017. p. 1198.

39. Cho J, Park H, Setsompop K, Bilgic B. Multi-shot Echo-planar imaging with simultaneous MultiSlice wave-encoding. In: Proceedings of the 27th Scientific Meeting of ISMRM. Montreal; 2019. p. 4768.

40. Cho J, Liao C, Zhang Z, et al. Highly accelerated EPI with wave encoding and multi-shot simultaneous MultiSlice imaging. In: Proceedings of the 28th Scientific Meeting of ISMRM. Online Conference; 2020. p. 4795.

41. Liao C, Cao X, Cho J, Zhang Z, Setsompop K & Bilgic B Highly efficient MRI through multi-shot echo planar imaging. In: wavelets and sparsity XVIII. Vol. 11138. International Society for Optics and Photonics; 2019. p. 1113818.

42. Polimeni JR, Bhat H, Witzel T, et al. Reducing sensitivity losses due to respiration and motion in accelerated echo planar imaging by reordering the autocalibration data acquisition: reducing losses in accelerated EPI with FLEET-ACS. *Magn Reson Med*. 2016;75:665-679.

43. Setsompop K, Fan Q, Stockmann J, et al. High-resolution in vivo diffusion imaging of the human brain with generalized slice dithered enhanced resolution: simultaneous multislice (gSlider-SMS). *Magn Reson Med*. 2018;79:141-151.

44. Hoge WS, Polimeni JR. Dual-polarity GRAPPA for simultaneous reconstruction and ghost correction of echo planar imaging data. *Magn Reson Med*. 2016;76:32-44.

45. Cauley SF, Setsompop K, Bilgic B, Bhat H, Gagoski B, Wald LL. Autocalibrated wave-CAIPI reconstruction; joint optimization of k-space trajectory and parallel imaging reconstruction. *Magn Reson Med*. 2017;78:1093-1099.

46. Beck A, Teboulle M. A Fast Iterative Shrinkage-Thresholding Algorithm for Linear Inverse Problems. *SIAM Journal on Imaging Sciences*. 2009;2:183-202.

47. Iyer S, Ong F & Doneva M, et al. SURE-based automatic parameter selection for ESPIRiT calibration. *Magnetic Resonance in Medicine*. 2020;84:3423-3437.

48. Wu W, Koopmans PJ, Andersson JLR, Miller KL. Diffusion acceleration with Gaussian process estimated reconstruction (DAGER). *Magn Reson Med*. 2019;82:107-125.

49. Hu Y, Wang X, Tian Q, et al. Multi-shot diffusion-weighted MRI reconstruction with magnitude-based spatial-angular locally low-rank regularization (SPA-LLR). *Magn Reson Med*. 2020;83:1596-1607.

50. Veraart J, Novikov DS, Christiaens D, Ades-aron B, Sijbers J, Fieremans E. Denoising of diffusion MRI using random matrix theory. *Neuroimage*. 2016;142:394-406.

51. Tournier J-D, Smith R, Raffelt D, et al. MRtrix3: a fast, flexible and open software framework for medical image processing and visualisation. *Neuroimage*. 2019;202:116137.

52. Smith SM, Jenkinson M, Woolrich MW, et al. Advances in functional and structural MR image analysis and implementation as FSL. *Neuroimage*. 2004;23:S208-S219.

53. Duyn JH, Yang Y, Frank JA, van der Veen JW. Simple correction method for k-space trajectory deviations in MRI. *J Magn Reson*. 1998;132:150-153.

54. Feinberg DA, Dietz P, Liu C, et al. Design and development of a next-generation 7T human brain scanner with high-performance gradient coil and dense RF. In: Proceedings of the 29th Scientific Meeting of ISMRM. Online Conference; 2021. p. 0562.

55. Breuer FA, Moriguchi H, Seiberlich N, et al. Zigzag sampling for improved parallel imaging. *Magn Reson Med*. 2008;60:474-478.

56. Cho ZH, Kim DJ, Kim YK. Total inhomogeneity correction including chemical shifts and susceptibility by view angle tilting. *Med Phys*. 1988;15:7-11.

57. Butts K, Pauly JM, Gold GE. Reduction of blurring in view angle tilting MRI. *Magn Reson Med*. 2005;53:418-424.

58. Hammernik K, Klatzer T, Kobler E, et al. Learning a variational network for reconstruction of accelerated MRI data: learning a

Variational network for reconstruction of accelerated MRI data. *Magn Reson Med*. 2018;79:3055-3071.

59. Aggarwal HK, Mani MP, Jacob M. MoDL: Model-Based Deep Learning Architecture for Inverse Problems. *IEEE Trans Med Imaging*. 2019;38:394-405.
60. Aggarwal HK, Mani MP, Jacob M, Aggarwal Hemant K., Mani Merry P. & Jacob M. MoDL-MUSSELS: Model-Based Deep Learning for Multishot Sensitivity-Encoded Diffusion MRI. *IEEE Transactions on Medical Imaging*. 2020;39:1268-1277.
61. Cho J, Tian Q, Frost R, Chatnuntawech I & Bilgic B Wave-encoded model-based deep learning with joint reconstruction and segmentation. In: Proceedings of the 29th Scientific Meeting of ISMRM. Online Conference; 2021. p. 1982.
62. Hebrank FX & Gebhardt M. Safe-model-a new method for predicting peripheral nerve stimulations in MRI. Proc Intl Soc Mag Res Med. 2000;8:2007.
63. Weaver JB. Simultaneous multislice acquisition of MR images. *Magn Reson Med*. 1988;8:275-284.

SUPPORTING INFORMATION

Additional supporting information may be found in the online version of the article at the publisher's website.

Figure S1. Auto-PSF simulation with system imperfections. The first row shows spatial frequency by 22 mT/m of one cycle cosine wave gradient. We simulated 40 us of time delay, 20% of gradient scaling error, and 10% of phase offset. The second row shows sparse contents of the Fourier transform of the spatial frequency. Time delay and scaling error of gradient changed the phase and amplitude of the sparse variables, respectively. Phase offset and other low-frequency contents will alter the amplitude of four sparse variables.

Figure S2. The effective wave gradient and spatial frequency at the 1 mm resolution imaging with 1516 Hz/pixel bandwidth. The last column shows the difference in the spatial frequency.

Figure S3. Fourier transform of wave-PSFs of standard wave-EPI and joint reconstruction. Standard wave-EPI reconstruction utilizes one wave-PSF for one slab while joint reconstruction uses wave-PSFs at the thin-slice resolution.

Figure S4. The number of 2nd-order crossing fibers according to the number of the keeping singular values during the SVD truncation for the low-rank regularization.

Figure S5. The reconstructed images, g-factor analysis, and tSNR maps of single-shot GE-EPI at $R_{in} \times R_{sms} = 4 \times 3$.

Figure S6. Single diffusion direction image with 1000s/mm^2 of b-value using the two-shot SE-EPI at $R_{in} \times R_{sms} = 5 \times 2$ per each EPI-shot.

Figure S7. 20 diffusion-direction DWI with 1000s/mm^2 of b-value using the single-shot SE-EPI at $R_{in} \times R_{sms} = 3 \times 2$ per each EPI-shot. Five different encoded RFs were used for high-resolution g-Slider.

Figure S8. The wave-encoding simulation for $1 \times 1 \times 1$ mm^3 voxel at bandwidth 1516 Hz/pixel. a. voxel signal simulation for the blipped-CAIPI b. voxel signal simulation with $24mT/m \times 12mT/m$ wave-encoding, where amount of wave-encoding was limited by the PNS limitation at the current 3 T Siemens system. The averaged g-factor was reduced by 1.09-fold at $R_{in} \times R_{sms} = 4 \times 3$ c: voxel signal simulation with $144mT/m \times 72mT/m$ wave-encoding for an advanced 7 T hardware system with head gradient coil,[54] where it has a similar PNS level with wave-EPI at the current 3 T Siemens system. The PNS was calculated by the SAFE model.[62] The averaged g-factor was reduced by 1.67-fold compared with the blipped-CAIPI. However, we observed the voxel tilting in the x-y domain[26,63] and blurring in the *x-z* domain, therefore, the FWHM of PSF was significantly increased to 3.06 mm. The simulation implies that the amount of wave-encoding might need to be constrained by the intra-voxel blurring in the wave-EPI acquisition as well as slew rate and PNS when using the cutting-edge hardware system. d. voxel signal simulation with $58mT/m \times 29mT/m$ wave encoding. When FWHM was limited by the 10% penalty, using the advanced hardware system still has the averaged g-factor gain by 1.30-fold compared with the blipped-CAIPI at $R_{in} \times R_{sms} = 4 \times 3$, which has 42% of PNS compared with the wave-EPI at the current 3 T Siemens system

Figure S9. (a) The optimal trajectory for image reconstruction at R2 imaging. Due to the readout oversampling, we can avoid the folding artifacts in the *x* direction and acquire missing lines without a time increase. However, this sampling pattern is not possible due to PNS and current hardware system. (b) Exemplar practical implementation using wave-CAIPI trajectory to reduce the effective reduction factor in the k_y direction with the current hardware systems while respecting PNS constraints. In the *x* direction, we can use the additional coil sensitivity variation to improve the reconstruction condition and readout oversampling boosts this advantage.

Figure S10. Exemplar k-space, aliased image (R = 2), signal from a single voxel (1.25×1.25 mm^2) after the image reconstruction, and PSF simulation for Cartesian sampling, acquisition with oblique readouts ($G_y = 30$ mT/m), and half-cycle wave encoding with $G_w = 30$ mT/m, respectively.

Figure S11. Phantom experiment for investigating the blurring caused by 29mT/m of half-cycle cosine wave gradients. The sizes of the pins in the phantom are 2.5, 2.0, 1.5, 1.0, 0.7, 0.5, and 0.4 mm. The center-to-center spacings of the pins are 5.0, 4.0, 3.0, 2.0, 1.4, 1.0, and 0.8 mm. We acquired 5 averages of 8-shot GE-EPI scans at reduction factor 8 and $1 \times 1 \times 5$ mm^3 of voxel resolution and

combined the shots before the image reconstruction. The bottom row shows the theoretical PSFs by wave-encoding gradients